High-resolution MCP-TimePix3 imaging/timing detector for antimatter physics

View the article online for updates and enhancements.

High-resolution MCP-TimePix3 imaging/timing detector for antimatter physics

L Glöggler[1,2,*], R Caravita[3,*], M Auzins[4], B Bergmann[5], R S Brusa[3,6], P Burian[5], A Camper[7], F Castelli[8], P Cheinet[9], R Ciuryło[10], D Comparat[9], G Consolati[11,12], M Doser[1], H Gjersdal[7], Ł Graczykowski[13], F Guatieri[6], S Haider[1], S Huck[1,14], M Janik[13], G Kasprowicz[13], G Khatri[1,7], Ł Kłosowski[10], G Kornakov[13], C Malbrunot[1], S Mariazzi[3,6], L Nowak[1], D Nowicka[13], E Oswald[1], L Penasa[3,6], M Piwiński[10], S Pospisil[5], L Povolo[3,6], F Prelz[12], S A Rangwala[15], B Rienäcker[1], O M Røhne[7], H Sandaker[7], T Sowinski[16], I Stekl[5], D Tefelski[13], M Volponi[1,6], T Wolz[1], C Zimmer[1,7,11,17], M Zawada[10] and N Zurlo[18,19]

[1] Physics Department, CERN, Geneva 23, 1211 Geneva, Switzerland
[2] Department of Physics, Technical University Berlin, Hardenbergstr. 36, 10623 Berlin, Germany
[3] TIFPA/INFN Trento, via Sommarive 14, 38123 Povo, Trento, Italy
[4] University of Latvia, Department of Physics, Raina Boulevard 19, LV-1586 Riga, Latvia
[5] Institute of Experimental and Applied Physics, Czech Technical University in Prague, Husova 240/5, 11000 Prague 1, Czech Republic
[6] Department of Physics, University of Trento, via Sommarive 14, 38123 Povo, Trento, Italy
[7] Department of Physics, University of Oslo, Sem Sælandsvei 24, 0371 Oslo, Norway
[8] Department of Physics, University of Milano, via Celoria 16, 20133 Milano, Italy
[9] Université Paris-Saclay, CNRS, Laboratoire Aimé Cotton, 91405 Orsay, France
[10] Institute of Physics, Faculty of Physics, Astronomy and Informatics, Nicolaus Copernicus University in Toruń, Grudziadzka 5, 87-100 Torun, Poland
[11] Politecnico of Milano, Piazza Leonardo da Vinci 32, 20133 Milano, Italy
[12] INFN Milano, via Celoria 16, 20133 Milano, Italy
[13] Warsaw University of Technology, Faculty of Physics ul. Koszykowa 75, 00-662 Warsaw, Poland
[14] Department of Physics, University of Hamburg, Jungiusstraße 9, 20355 Hamburg, Germany
[15] Raman Research Institute, C. V. Raman Avenue, Sadashivanagar, Bangalore 560080, India
[16] Institute of Physics, Polish Academy of Sciences, Aleja Lotnikow 32/46, PL-02668 Warsaw, Poland
[17] Department of Physics, Heidelberg University, Im Neuenheimer Feld 226, 69120 Heidelberg, Germany
[18] Department of Civil, Environmental, Architectural Engineering and Mathematics, University of Brescia, via Branze 43, 25123 Brescia, Italy
[19] INFN Sezione di Pavia, via Bassi 6, 27100 Pavia, Italy

E-mail: lisa.gloggler@cern.ch and ruggero.caravita@cern.ch

CrossMark

Abstract

We present a hybrid imaging/timing detector for force sensitive inertial measurements designed for measurements on positronium, the metastable bound state of an electron and a positron, but also suitable for applications involving other low intensity, low energy beams of neutral

---

* Authors to whom any correspondence should be addressed.

(antimatter)-atoms, such as antihydrogen. The performance of the prototype detector was
evaluated with a tunable low energy positron beam, resulting in a spatial resolution of ≈ 12 mm,
a detection efficiency of up to 40% and a time-resolution in the order of tens of ns.

(Some figures may appear in colour only in the online journal)

1. Introduction

Performing the first inertial studies with low energy neutral antimatter atoms [1] is the main goal of the AEḡIS collaboration, located at the CERN Antiproton Decelerator. Of particular interest is determining the gravitational acceleration experienced by anti-atoms in Earth's gravitational field from their non-relativistic motion inside a so-called Moiré deflectometer [2]. The measurement concept consists in working out the average acceleration experienced by the atoms from their non-relativistic equation of motion in the deflectometer, $\delta y = a\delta t^2$, where δy is the acquired vertical displacement after the free-fall and δt is their time of flight throughout the device. One method is to adopt a pulsed beam of anti-atoms with a time spread in the order of tens of ns and detect δy and δt on the same sample. If two independent detectors are employed for the two quantities, no correlated event identification is possible between individual δy and δt measurements. The acceleration can only be determined by statistically averaging the collected δy and δt samples and solving their average equation of motion. Contrarily, if an event correspondence between δy and δt measurements can be reliably obtained, the possibility of working out the acceleration for each event is attained. This opens the possibility to measure the statistical distribution of acceleration values and study its correlations with other experimental parameters.

Pulsed inertial sensing experiments employing neutral anti-atoms are now conceivable due to recent successes in forming both antihydrogen ($\overline{H}$, the bound state of a positron and an antiproton) and positronium (Ps, the bound state of a positron (e^+) and an electron) with time-controlled processes. In the former case, a pulsed source of $\overline{H}$ atoms was recently demonstrated, producing anti-atoms in a 250 ns-wide time window by a charge exchange reaction with Rydberg-excited positronium atoms, having an axial root mean square velocity of ≈ 2000 m s^{-1} [3]. In the latter case, pulsed positronium sources are routinely obtained by implanting pulsed e^+ bunches in suitable matter converters [4]. Typical formation velocities of positronium (0.7–1.0×10^{-5} m s^{-1}) [5] are much higher than the ones of $\overline{H}$ due to the small weight of positronium. However, positronium sources feature much shorter production time windows (8–20 ns) [6] thanks to the higher degree of control over positron bunches reached by employing modern plasma-based positron trapping techniques [7]. In both cases, average pulse durations are much shorter than the atoms' average time of flights along a typical 30–100 cm baseline necessary to host a Moiré deflectometer, allowing the conceptual design of the first experiments

adopting pulsed sources and this kind of inertial-sensing devices [8, 9].

An effective deflectometer/detector assembly design in terms of efficient usage of the low flux atomic beams from these sources consists of a two-grating deflectometer complemented by a combined position- and time sensitive sensor. Its spatial resolution needs to be high enough to resolve the deflectometer fringe pattern, while the timing resolution should allow for an accurate determination of the time of flight of each atom. In the proposed experimental designs aiming at measuring the gravitational acceleration of $\overline{H}$, for instance, $\delta y \ll 10$ mm and $\delta t \ll 1$ µs [8]. At present, spatial resolutions of ≈ 1 mm to antiproton annihilations can be reached only by nuclear emulsion detectors [10], which however offer no timing resolution and real-time diagnostics.

One possibility to realize a combined position- and timing-sensitive detector is to exploit annihilation processes occurring when anti-atoms impact material obstacles. High energy annihilation products (charged/neutral pions and nuclear fragments for $\overline{H}$, gamma rays for Ps) can be detected with pixelated high energy detection systems allowing annihilation vertex reconstruction while providing accurate time resolution. This approach has proven successful to provide combined position- and time detection of $\overline{H}$ atoms, due to the high average number of annihilation products (on average 2.8 charged pions are emitted per annihilation event) and their high detection efficiency with a modest material budget. Several collaborations have developed hybrid vertexing/timing detectors for antihydrogen. Examples are ATHENA, ALPHA and AEḡIS, whose detectors reached spatial resolutions in the order of a few mm [11–13]. Pursuing this approach is more difficult in the case of positronium, where either two 511 keV (para-Ps) or three 0–511 keV (ortho-Ps) gamma rays are emitted per annihilation. On the one hand, efficiently detecting high energy gamma rays typically requires scintillation detectors in the range of several cm to provide sufficient stopping power, which limits its spatial resolution. On the other hand, the limited number of emitted gamma rays imposes stringent efficiency limits due to the necessity of building coincidences to reconstruct vertices. One notable detector example is J-PET [14], which reached a 5 mm resolution and a vertexing efficiency of 0.1% to ortho-Ps annihilations, having however a diameter of ≈ 1 m.

An alternative approach consists of field- or photoionizing the atoms. Low energy charged antiparticles such as positrons and antiprotons can be detected by microchannel plates (MCP) with phosphor screens [15] and a field ionization detector for the study of Rydberg positronium has been developed [16].

This approach is particularly convenient when implemented within the volume of electromagnetic traps, as those used in antimatter experiments.

The magnetic field radially confines charged particles by cyclotron motion, allowing macroscopic separation between dissociation and detection planes. This approach was pioneered recently by the AEḡIS collaboration, which first demonstrated a hybrid imaging and timing photoionization MCP-phosphor detector operated in a 1 T magnetic field [17]. The detector featured a dual acquisition chain: a CMOS camera readout to acquire the time-integrated image of the phosphor screen, and a fast electronic readout of the space-integrated electric signal of the phosphor screen. It reached 88 μm spatial and 15 ns timing resolution in the imaging plane [18]. This proof-of-concept detector, however, also exhibited some limitations hampering its adoption in a first inertial sensing experiment. Primarily, the incapability of distinguishing individual hits in the electric signal, due to the limited bandwidth and signal-to-noise ratio of the collective readout and the intrinsic spatial resolution limit imposed by the imaging system. Furthermore, even if a better design of the readout chain would improve the first issue, the independence of the two acquisition chains would necessitate to operate the detector in the single particle detection regime. A way to surpass these limitations consists in replacing the two separate and independent acquisition chains by a more sophisticated detection system to simultaneously obtain the position and the timing of each event at once.

In both antihydrogen and positronium, the embedding of an ionization stage in the present detector layout has a central role to enable experimentation with neutral anti-atoms. Possibilities are either an intense laser beam in front of the first MCP layer or a metallic grid structure with a strong electric field, or a combination of the two. Positrons released by ionization would have to be guided towards the detection module by either a strong magnetic field perpendicular to the detector surface (as in [17]) or by a guiding electric field (as in [16]).

In this article, we present a novel hybrid position and timing detector featuring simultaneous 12 μm imaging and 15 ns timing resolution, an up to 41% detection efficiency of low energy antimatter-matter systems' ionization products and individual event identification. This detector is based on the combination of a MCP and a TimePix3 pixel detector used as readout anode, previously demonstrated in [19–21]. The capabilities and advantages of combining MCP detectors with Medipix/TimePix readout are summarized in [22]. A testing campaign was conducted with a tunable low energy positron beam to study its capabilities in detecting positrons in the energy (velocity) range compatible with both, antihydrogen and positronium photo- and field-dissociation events.

2. Detection module

The detection module studied here is schematically depicted in figure 1. It consists of a MCP stack in chevron configuration read out by a TimePix3 application specific integrated circuit (ASIC) [23], used as a capture anode for the electron bursts emerging from the MCPs. A negative potential in the kV range is applied to the MCP front face to attract low energy positrons. Impacting positrons with a few keV efficiently release secondary electrons in the first section of the MCP channels, which are subsequently amplified by the accelerating electric field in the MCP channels. The electron clouds emerge into the gap between the TimePix3 and the MCP stack and are accelerated by the uniform electric field between the MCP backside and the TimePix3 surface, which is connected to ground by the front-end readout electronics of each of its pixels' pads. When the electron clouds hit the surface of TimePix3, their transverse projection typically covers multiple pixels. This is caused by the expansion they experience during the flight in the gap between the MCP stack and the TimePix3 chip, driven by the Coulomb repulsion of the electrons in the charge cloud. For this effect, and due to the TimePix3 feature of measuring the pixel-per-pixel absolute charge deposit, sub-pixel size spatial resolution of the impact position is achievable by means of centroid reconstruction algorithms, applied to each detected charge cloud.

In the current detector configuration, the positrons are imaged by two MCPs (18-10, TopAG Lasertechnik GmbH) in chevron configuration. In this configuration, the relative angle between pores of neighbouring plates is maximized, which reduces undesirable ion feedback by forcing the ions to hit the channel walls instead of propagating all the way through the channel and release another electron avalanche at the surface of the MCP. An aluminum spacer between the two MCP plates creates a gap of 300 μm. Each plate has a thickness of 0.43 mm, an active area of 18.6 mm and an open area ratio of $\geqslant 58\%$. The channel diameter is 10 μm and the inter-channel distance is $\leqslant 12$ μm. The electron gain is $\geqslant 10^3$ for each individual plate at a voltage of 0.8 kV between the front face and the back face of the MCP. The readout ASIC is mounted at a distance of ≈ 4 mm from the MCP stack. With TimePix3 at ground, the voltage applied to the back face of the second MCP plate in the chevron stack determines the acceleration of the electron cloud emitted by the MCP stack. TimePix3 is a hybrid pixel detector readout chip based on 130 nm CMOS technology, developed by the Medipix3 collaboration at CERN Pixels with a size of 55×55 μm^2 are arranged in a matrix of 256×256, forming an area of 14×14 mm^2. The chip is operated in data-driven readout mode, where individual pixels are read out when triggered while the rest of the pixel matrix remains active. TimePix3 allows the simultaneous measurement of time-over-threshold (ToT), which is an output value proportional to the charge collected by the pixel, and the time-of-arrival (ToA) with a resolution of 1.56 ns (640 MHz). The TimePix3 analog front-end consists of an input pad, a preamplifier with a leakage current compensation circuit, a digital-to-analog converter and a discriminator. The charge collected by a pixel is integrated and preamplified. If the output voltage of the preamplifier exceeds a threshold, a pulse is generated by the discriminator, which starts the clock. The pulse length corresponds to the time the preamplifier output voltage is larger than the threshold. The chip is read out with Katherine, an ethernet embedded readout interface for TimePix3 [24]. The chipboard is directly connected to the readout device with a
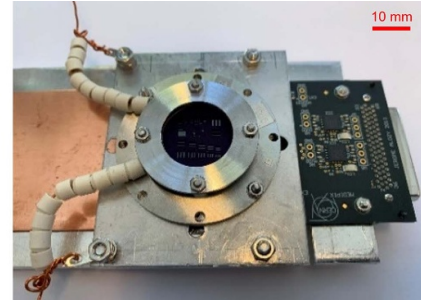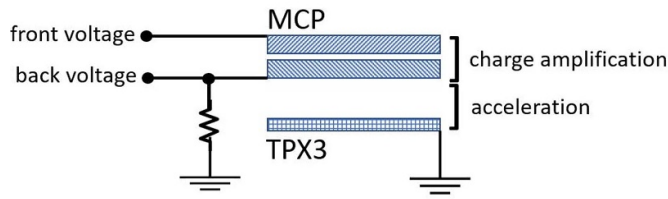
Figure 1. Left: conceptual scheme of the detector, showing the MCP stack and the TimePix3 and their electrical connections. Right: detection module.

VHDCI (Very-High-Density-Cable-Interconnect) 68-pin connector. TimePix3 dissipates 1.5 W of power. To ensure temperature stability of the chip during operation, the back side of the chipboard is in contact with a water heat exchanger via a copper plate and copper pipes.

3. Experimental characterization

The detection module was characterized in terms of detection efficiency, spatial resolution and time resolution. In the following, the experimental setup and data processing procedures are described and the results are discussed.

3.1. Positron beamline used for characterizing the detector

The detector assembly was experimentally tested with the continuous e^+ beam from the electrostatic positron beamline of the AML (AntiMatter Laboratory) of the University of Trento. The beam is tunable between 50 eV and 25 keV while keeping the sample under study at ground potential. The beam line is schematically depicted in figure 2 and thoroughly described in [25]. Briefly, positrons emitted by a 12 mCi Na^{22} source and moderated by a tungsten foil are electrostatically transported, collimated and accelerated towards a sample region held at ground potential. This is achieved by biasing a set of low voltage beam shaping electrodes together with their power supplies to high DC potential in the 50 V–25 kV range. An insulation transformer connected to the 220 V AC mains provides the necessary isolation to the DC low voltage power supplies, while a ceramic section of the vacuum chamber effectively isolates the beam-forming region to the sample chamber. The beam size at the target position is roughly 1–2 mm in full-width at half maximum for all beam energies; its alignment also does not vary by more than ≈1 mm while spanning from 200 eV to a few keV [25]. These are very suitable conditions for the present characterization, as the TimePix3 chip features a 14×14 mm^2 overall size encompassing the entire beam spot. Fine beam steering corrections (in both horizontal and vertical axes) could optionally be performed by adding discrete magnetic correctors right before the sample chamber, altering the e^+ trajectory by the little amounts needed to either center the beam on specific positions of the detector surface, or to compensate slight positional variations during energy scans. Typically, this beamline
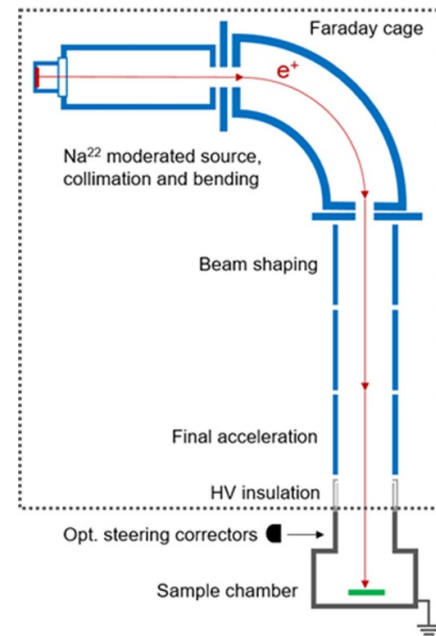

Figure 2. Schematic drawing of the electrostatic positron beamline used to characterize the detection module. Components highlighted in blue are held at a high DC negative voltage between 0 and 25 kV, whereas the sample chamber is kept at ground potential by insulating it from the acceleration stage with a ceramic vacuum section.

delivers positrons with a constant rate in the 4–8×10^4 e^+s^{-1} range. This range does not stem from intensity fluctuations: it is linked to the intrinsic degradation of the nominal moderation efficiency from the tungsten foil moderator after exposures to ambient pressure and due to rest gas in the vacuum. A high temperature re-activation cycle is required to recrystallize the tungsten foil after every exposure, and slight moderation efficiency variations up to ±30% are normally observed between different activation cycles.

3.2. Raw data processing

In a first step, the time of arrival is calculated in ns and the pixel numbers are converted to cartesian coordinates. The event list is sorted by increasing ToA values. To identify pixels belonging to the same cluster of pixels, according to the flux of the
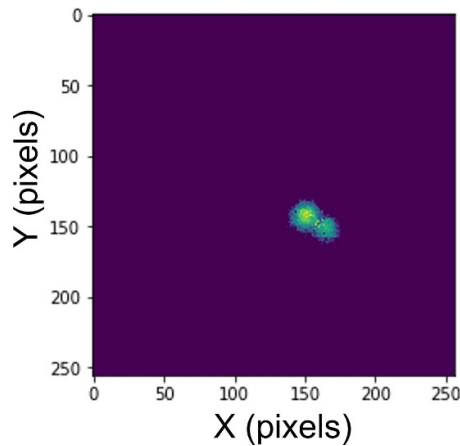
Figure 3. Overlapping footprints of two positron events in one time frame.

positron beam, a coincidence time window in the order of a few μs is chosen. All pixels hit within that time window are interpreted as belonging to the same cluster. A minimum cluster size in the order of about 20 pixels (depending on the MCP gain- and acceleration voltages) is set as a threshold to discriminate noise. Clusters containing less pixels than the minimum cluster size are rejected. Both, the length of the coincidence time window and the minimum cluster size depend on the acceleration voltage and the gain of the MCP stack. For each set of these parameters the coincidence window and the minimum cluster size needs to be optimized. A compromise needs to be found between a coincidence window long enough to avoid clusters being sliced and interpreted as several clusters of pixels and short enough to prevent event overlaps (figure 3) in one timeframe. Event overlaps cannot be discriminated by the algorithm and the center-of-mass of the combination of the footprints is calculated. This is a systematic error in the analysis. With optimized settings, event overlaps can be reduced to 1%–2% of the total events. The minimum cluster size needs to be set large enough not to account for cluster fractions resulting from cluster slices falsely distributed over different time frames and to discriminate noise. However, with an increasing minimum cluster size more events are being falsely rejected. This process returns a list of clusters, each cluster containing the pixels triggered, the coordinates of the pixels and their corresponding ToA and ToT values.

4. Results and discussion

4.1. Background event rate

An initial background measurement campaign was conducted to estimate the rate of background events observed by the detector, not attributable to positron impacts. The measurement was performed by inhibiting the transport of positrons towards the detector by turning off the high-voltage power supply biasing the electrostatic 90° bender in the beamline. All other power supplies were left to their nominal setting, including the main high voltage biasing the beam line set at 1.0 kV, to

allow transporting eventual spurious positive ions originating from the vertical section of the transfer line, thus allowing a more inclusive estimation of the rate of background events on the detector.

A background count rate of $17\,\mathrm{s}^{-1}$ was observed, integrating over the whole surface of the TimePix3 chip. This measured background rate, if compared to the typical detection rate when positrons are transported in the order of $\approx 10^4\,\mathrm{s}^{-1}$, is completely negligible for the purpose of this work to characterize the resolution and efficiency of the detection module. These detected background events were most likely either positive ions originating in the transfer line and transported onto the detector, cosmic ray events and thermally-excited electron avalanches in the MCP stack. Shot-noise of TimePix3 was found to be completely negligible, thanks to the high trigger threshold that could be programmed in a way not to impact the efficiency in detecting MCP avalanches.

4.2. Cluster size distribution

The electron clouds emerging from the channels of the MCP stack leave a circular shaped charge footprint. The size (number of active pixels) of these electron clusters strongly depends on the MCP gain voltage and the acceleration voltage across the gap between the MCP stack and TimePix3. Figure 4 shows the cluster size distribution for varying beam energies, acceleration voltages and MCP gain voltages, respectively. Selections were applied to only take into consideration clusters larger than 20 pixels and smaller than 500 pixels, to reject cluster fragments and event overlaps. The distributions were built from sample sizes of 10 000 clusters.

Higher positron beam energies increase the probability of creating secondary electrons at the surface of the first MCP, which reflects in a slight increase in the number of large clusters, whereas smaller and medium sized clusters seem to be equally distributed for different beam energies. An increase in MCP gain voltage leads to higher amplification in the channels, thus more electrons in the charge clouds and stronger Coulomb repulsion. The charge cloud size in the plane of the chip significantly gets larger with increasing MCP gain voltage, which can be seen in the corresponding histogram. The distributions also show an increase in cluster size with higher acceleration voltages. This can be explained by the electrons with increased kinetic energy having a higher chance to activate a pixel, thus the former dark border of the electron cloud becomes visible. This is a systematic effect of the detector.

4.3. Positron detection efficiency

To obtain the number of positrons hitting the detector surface during a given time interval with high precision, the photons emitted upon positron annihilation at the surface of the detector were measured with a NaI(Tl) scintillator (Scionix 76B76/3M) coupled to a photomultiplier tube (Canberra 2007P). The scintillator was calibrated with a Na^{22} source of known activity, mounted close to the detection
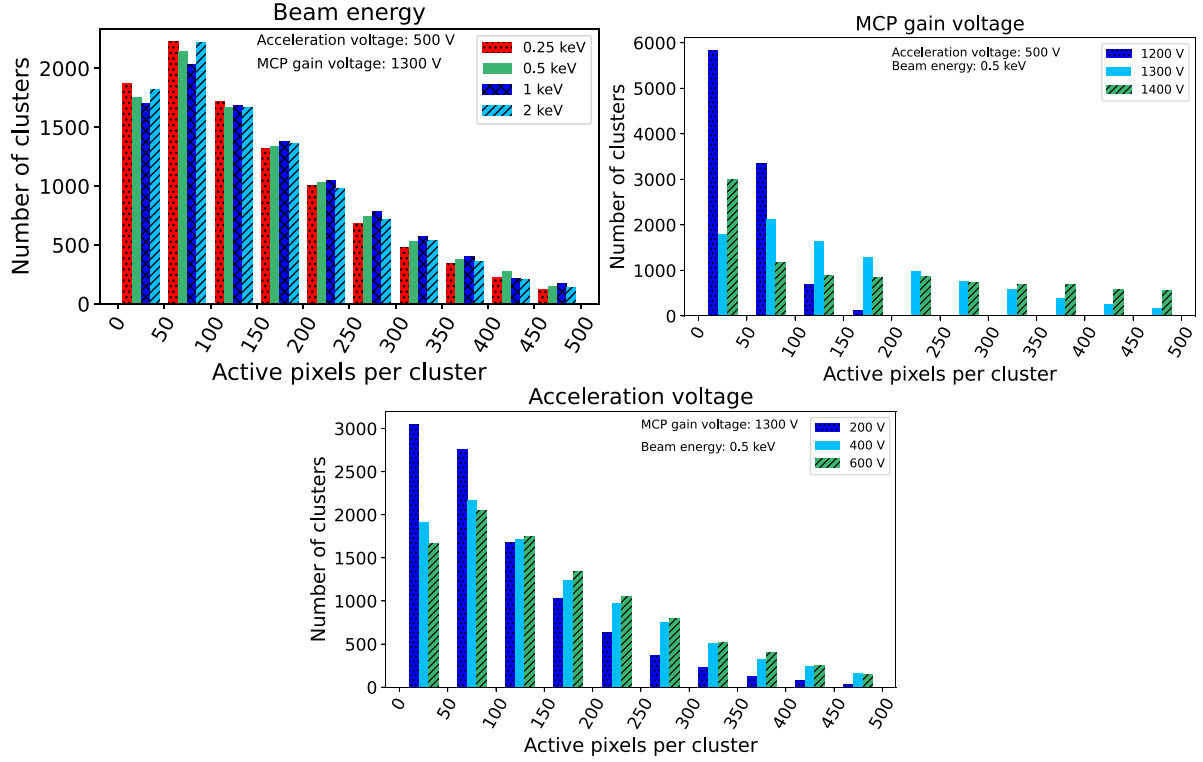
Figure 4. Cluster size distribution as a function of positron beam energy, acceleration voltage and MCP gain voltage, respectively. If not specified, the acceleration voltage was 500 V, the MCP gain voltage 1300 V and the beam energy 0.5 keV.

Table 1. Detection efficiency in % as a function of MCP gain voltage and acceleration voltage at a positron beam energy of 0.5 keV. The errors are statistical.

Acceleration voltage	MCP gain voltage				
	1200 V	1250 V	1300 V	1350 V	1400 V
100 V			< 1	< 1	3.9 ± 0.8
200 V		< 1	1.9 ± 0.4	9.8 ± 1.4	23.7 ± 1.9
300 V		< 1	8.5 ± 1.3	20.1 ± 1.6	32.6 ± 1.6
400 V	< 1	2.4 ± 0.5	12.7 ± 1.3	26.2 ± 1.7	37.4 ± 1.6
500 V	< 1	4.9 ± 0.7	17.6 ± 1.8	31.5 ± 1.6	40.4 ± 0.8
600 V	< 1	7.1 ± 1.1	20.1 ± 1.6	33.0 ± 1.7	41.1 ± 2.1

module and facing the surface of the first MCP. The calibration procedure yielded the photopeak detection efficiency DE_γ at 511 keV of the scintillator.

Varying the parameters beam energy, acceleration voltage and MCP gain voltage, for each set of parameters data was taken simultaneously with the MCP-TimePix3 detection module and the scintillator. For each measurement, the number of counts N_γ in the 511 keV gamma peak was extracted from the spectra. With a factor of 2 accounting for the two produced photons per positron annihilation event, the number of positrons delivered by the AML positron beamline in each time interval is:

$$N_{e+} = \frac{N_\gamma}{2 \cdot DE_\gamma}. \quad (1)$$

The positron detection efficiency of the detection module DE_{e+} was calculated as the ratio of the rate of clusters registered by the detector N_{clusters} and the rate of positrons delivered N_{e+}:

$$DE_{e+} = \frac{N_{\text{clusters}}}{N_{e+}}. \quad (2)$$

The detection efficiency is limited by the open-area-ratio (OAR) of the MCPs and the probability of a positron to produce a secondary electron at the MCP front face. The probability of the algorithm to correctly interpret a cluster of pixels as an event also plays an important role. Table 1 shows the detection efficiency in % for different MCP gain voltages and acceleration voltages at a positron beam energy of 0.5 keV.

Figure 5 shows that the detection efficiency strongly increases with both, MCP gain voltage and acceleration voltage, respectively. Higher MCP gain voltages lead to more amplification and larger electron clouds emerging from the MCP stack. These are more likely to trigger the minimum
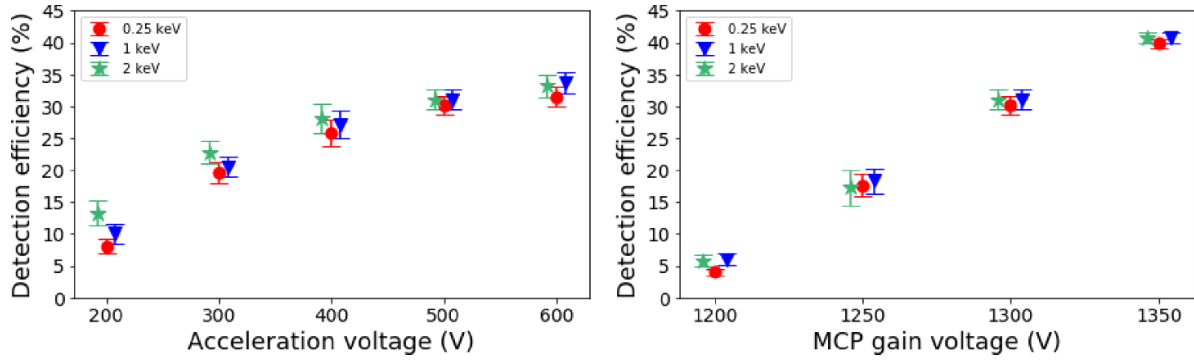
Figure 5. Detection efficiency in % as a function of MCP gain voltage and acceleration voltage, respectively, at positron beam energies of 0.25 keV, 1 keV and 2 keV. For better distinguishability of the individual data points, an offset of 8 V on the voltage axis has been introduced artificially between the data sets belonging to different beam energies. The MCP gain (acceleration) voltage was kept at 1300 V (500 V) during the scan of the acceleration (MCP gain) voltage.

number of pixels necessary for a cluster to be interpreted as a positron event by the algorithm than smaller electron clouds. The charge cloud effective diameter scales as the square root of the acceleration voltage [26]. This relation also reflects in the detection efficiency, as can be observed in figure 5(left). Slightly increased detection efficiencies are expected with higher beam energies, which can be attributed to the probability of secondary electron creation being higher with larger beam energies.

4.4. Spatial resolution

To obtain sub-pixel spatial resolution, a centroiding algorithm was applied to calculate the center-of-mass of each cluster. An image of a sharp knife edge was used to determine the spatial resolution of the detection module.

4.4.1. Centroiding algorithm.
The center-of-mass is extracted from each cluster identified in the first step of the analysis procedure described in section 3.2. Therefore, for each pixel the ToT value, proportional to the deposited energy, is integrated over the entire time interval of the cluster. With the pixel numbers converted into cartesian coordinates, the ToT values are summed for each pixel along the *X*- and *Y*-axis, respectively. This yields two histograms proportional to the charge distribution across the chip. The mean values of these histograms are taken as the center-of-mass coordinates of the cluster. The process is illustrated in figure 6.

4.4.2. Edge spread function.
The spatial resolution of the detection module was determined with the edge spread function (ESF) method. The ESF is the response of a system to a high contrast edge. To obtain an image of a sharp edge, half of the MCP surface was covered with a fine metal blade. The metal blade was positioned parallel to the MCP surface, with a 300 μm aluminum spacer between the blade and the MCP to avoid damaging the MCP. With increasing distance between the MCP and the knife edge, the spatial resolution is expected to get worse, however this has not been tested experimentally.

The blade was kept at the same potential as the front face of the first MCP plate.

The image of the edge was reconstructed, applying the centroiding algorithm described above to all clusters. The intensity along the edge within a subset of the image is then integrated and fitted with an error function:

$$y = a + \frac{b}{2}\left[\mathrm{erf}\left(\frac{x_0 - x}{\sigma\sqrt{2}}\right) + 1\right]. \tag{3}$$

This process is illustrated in figure 7. The resolution is extracted from the parameters of the fit by multiplying σ with the pixel size of 55 μm.

4.4.3. Results.
Displayed in table 2 are the results as a function of MCP gain voltage and acceleration voltage between the MCP back face and TimePix3, taken at a positron beam energy of 0.5 keV. The errors are statistical. Figure 8 shows the spatial resolution as a function of the acceleration voltage and MCP gain voltage, respectively. Higher acceleration voltages lead to better spatial resolutions. The minimum is reached at around 12 μm, corresponding to the inter channel distance of the MCPs. The MCP gain voltage seems to have no significant influence on the spatial resolution.

5. Time resolution

The timing resolution of the detector was estimated by studying the distribution of the active pixels in time per detected electron avalanche.

A set of several thousand individual clusters with the same acceleration and gain conditions was collected, and each cluster's starting time was defined by the time of the first pixel firing (i.e. the minimum ToA value in the cluster). The distribution of active pixels per time bin was constructed by summing over the number of active pixels in the [ToA, ToA+ToT] interval in steps of 1.56 ns. The distribution was normalized by the number of clusters in the sample.

Figure 9 shows the average number of active pixels in an individual typical electron avalanche. Three main structures
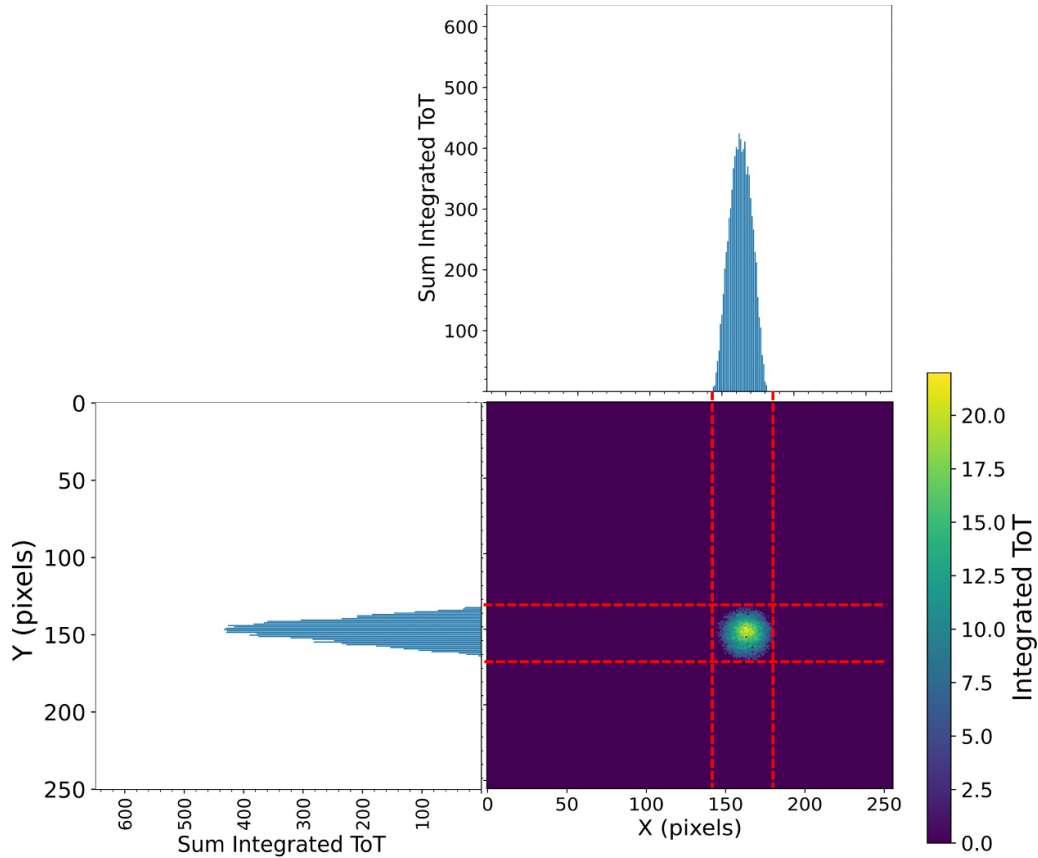
Figure 6. Reduction process from one cluster to the coordinates of its centroids: the charge deposited on the chip is integrated for all pixels along the *X*- and *Y*-axis respectively. The mean value of the resulting distributions is calculated and used as *X* and *Y* coordinate of the center-of-mass of the cluster.
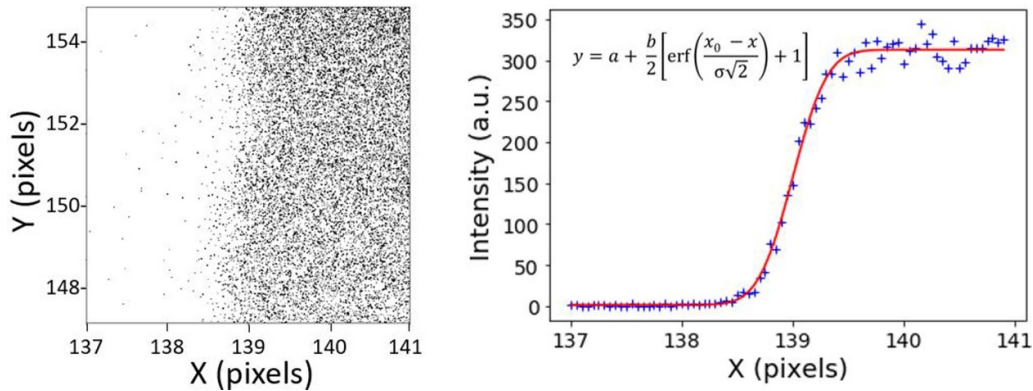

Figure 7. On the left a subset of an image of a sharp edge is shown. This image is composed of the center-of-mass coordinates of the clusters. Integrated along the *X*-axis, the resulting intensity profile is fitted with an error function. Multiplication of the fit parameter σ with the pixel side length of 55 µm yields the spatial resolution of the detector.

are identified: a first primary pulse lasting up to 24 ns after the cluster starting time, a secondary pulse starting at about 24 ns and lasting until 62 ns, and a tertiary pulse after 62 ns. Each of these structures is related to a different spatial distribution of pixels firing (shown in figure 9, insets): the first pulse involves mainly pixels corresponding to the center of the cluster, whereas the second and the third pulse pixels are distributed in a ring-shaped corona around the pixels of the first pulse.

These observations can be explained by ion feedback in the MCP stack and the dead time of the TimePix3 pixels. MCP detectors can give rise to afterpulses due to positive ion feedback propagating backwards in the channels and producing delayed, secondary avalanches [27]. These secondary avalanches are spatially aligned with respect to the primary avalanche, despite being separated in time by the round-trip of the ion avalanche in the MCP stack, typically between a few ns to few 100 ns after the first signal. This round-trip time, on the

Table 2. Spatial resolution in μm as a function of MCP gain voltage and acceleration voltage at a positron beam energy of 0.5 keV. The errors are statistical.

Acceleration voltage	MCP gain voltage				
	1200 V	1250 V	1300 V	1350 V	1400 V
100 V			20.2 ± 1.6	20.3 ± 1.8	16.8 ± 1.5
200 V		13.4 ± 1.6	14.1 ± 0.7	14.6 ± 0.5	16.8 ± 0.7
300 V	15.3 ± 1.1	14.3 ± 0.7	12.8 ± 0.4	14.7 ± 0.5	14.3 ± 0.9
400 V	13.3 ± 0.9	12.0 ± 1.4	14.3 ± 0.9	12.6 ± 0.4	16.2 ± 0.6
500 V	12.4 ± 1.3	12.6 ± 0.5	11.3 ± 0.9	13.5 ± 0.9	13.9 ± 0.5
600 V	11.8 ± 0.7	10.5 ± 1.1	11.9 ± 0.4	11.1 ± 0.3	12.5 ± 0.6
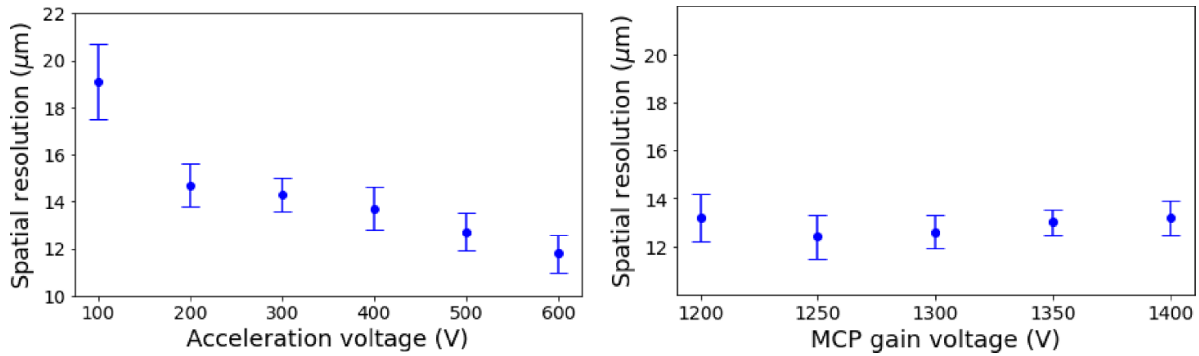
Figure 8. Spatial resolution in μm as a function of acceleration voltage and MCP gain voltage, respectively, at a positron beam energy of 0.5 keV. In the plot on the left (right), for each acceleration voltage (MCP gain voltage) data point, the resolution was averaged over all corresponding MCP gain voltages (acceleration voltages). The MCP gain (acceleration) voltage was kept at 1300 V (500 V) during the scan of the acceleration (MCP gain) voltage.

other hand, is shorter than the pixel dead time of the TimePix3 chip of 475 ns [23]. This implies that the core of the secondary avalanche cannot be detected by pixels that have fired in the primary avalanche, which are still recovering. Only the outer corona of the secondary avalanche is effectively detected, as a consequence of the overall charge accumulation from the primary avalanche and the secondary avalanche. The same principle applies to further avalanches.

Several ways are possible to estimate the average spread of the time distribution and work out an estimate of the time resolution of this detector in determining the time of impact of isolated events. Conservatively, one can consider the whole time distribution in figure 9 and estimate the resolution from its whole standard deviation, leading to a time resolution in the order of ≈40 ns. Alternatively, one can apply a cut at 25 ns and isolate only the pixels from the first pulse, while rejecting those that were most likely triggered by an ion-feedback avalanche. This second approach pinpoints that a more accurate estimate of the time resolution of isolated events is 12–15 ns.

The observed timing spread of the first avalanche is likely to originate from the energy spread of the electrons as they get amplified within the channels and space charge effects during their accelerated flight in the gap between the MCP stack and the TimePix3 chip. It has to be noted that the time-walk effect of the TimePix3 pixels is also likely to contribute to a broadening of the distribution, as different pixels in the cluster reach the triggering threshold at different times. Methods to compensate for such time-walk effects with TimePix3 are known in literature [28], yet their study
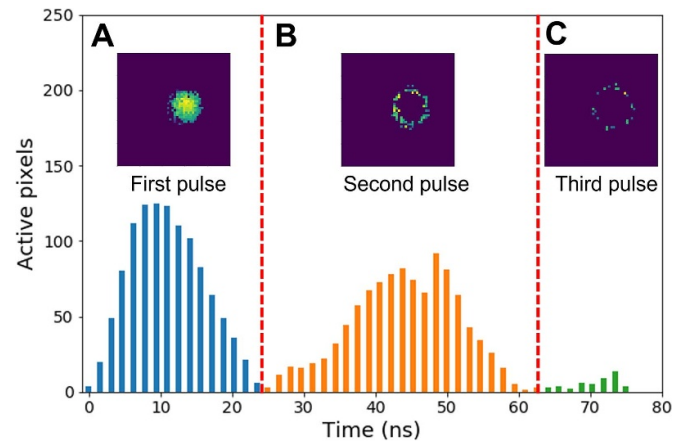
Figure 9. Evolution of the number of active pixels during the registration of one electron cloud (corresponding to one individual positron event).

in the present case, as well as an accurate simulation of the electron effects in the channels, goes beyond the scope of this experimental first investigation and will be subject of future studies.

The time resolution was extracted from the first 25 ns in the pulse by calculating the standard-deviation of the distribution, averaging over several thousands of such pulses (with the same MCP gain voltage, acceleration voltage and beam energy). The pulse was normalized by the number of clusters of the sample. For samples of different MCP voltage settings
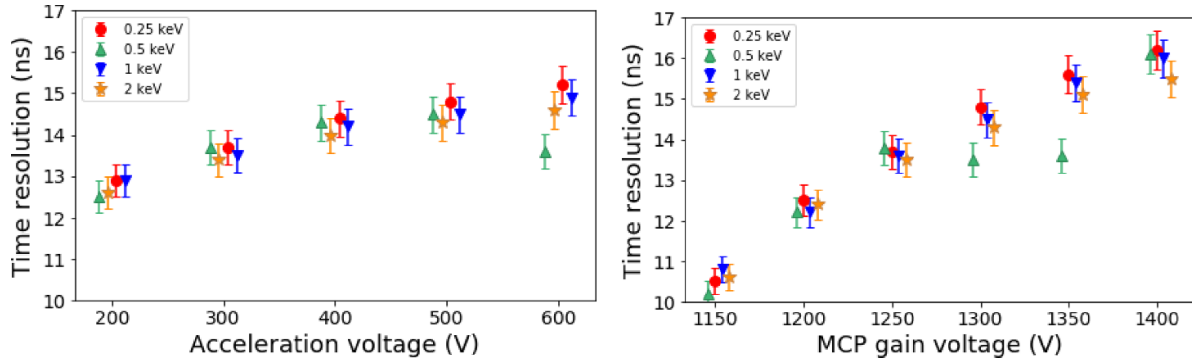
Figure 10. Time resolution as a function of acceleration voltage and MCP gain voltage, respectively, for different beam energies. For better distinguishability of the individual data points, an offset of 8 V on the voltage axis has been introduced artificially between the data sets belonging to different beam energies. The MCP gain (acceleration) voltage was kept at 1300 V (500 V) during the scan of the acceleration (MCP gain) voltage.

and beam energies, the amplitude of the pulses varies slightly with the average cluster size. The errors are statistical.

The time resolution was studied as a function of the acceleration voltage between the MCP stack and TimePix3, as a function of the MCP gain, and for different energies of the positron beam (shown in figure 10). A worsening of the time resolution was observed for higher MCP gain- and acceleration voltages, linked to the increase of the average cluster size. No significant dependence upon the positron beam energy was observed.

Finally, we want to emphasize that this assessment aimed at determining the precision of this detector in timing isolated events, giving no information about its absolute accuracy. In fact, no measurement could be performed to measure the travelling time from the positron impact at the surface of the first MCP plate to the TimePix3 chip. This would require an external timing signal finely calibrated with the positron impact on the detector plane, unavailable on a continuous positron beamline relying on stochastic nuclear disintegrations. An experiment like such would require a ns-pulsed positron source, such as that of AEḡIS [6].

6. Conclusion and outlook

In this work, we have demonstrated a high resolution imaging detector for low energy positrons featuring single event tagging and simultaneous position and timing readout. This detector is based on the combination of a MCP and a TimePix3 integrated circuit, providing for each pixel the precise ToA and total charge deposit given as the ToT. This hybrid detector combines the high detection efficiency to incoming low energy charged particles of MCPs with the high timing and spatial resolution of the TimePix3 readout anode. A characterization campaign conducted on a low energy positron beamline showed that spatial and timing resolutions of $\delta y \approx 12$ μm and $\delta t \approx 12$–15 ns can be simultaneously achieved in combination with a 41% total detection efficiency, i.e. 71% probability that a positron generates a secondary electron avalanche, if one accounts for the 58% open area ratio. The availability of this tool opens several new possibilities in the antimatter research

field. One area of impact are experiments dealing with accurate determination of the impact of positrons. The enhanced spatial resolution of this method compared to known MCP-phosphor screen designs for positron physics, typically above 50 μm [17, 29], make it appealing, for instance, for positron interferometry [30]. Another area are inertial studies with antihydrogen or positronium, where accurate event-by-event determination of position/timing of positron impacts is of high relevance. Indeed, most proposed inertial schemes to date are based on a free-falling region and detectors sampling the atoms impact positions and time of flights, such as in [8] or [9]. Both antihydrogen and positronium can either be field [31] or photoionized [17], leading to low energy detectable positrons. The detector presented here would allow working out *g* from gravitational displacement laws of the type $y = kgt^2$ on an event-by-event basis[20], allowing the distribution of *g* values to be empirically determined and the different contributions from δy and δt to the total error budget $\delta g^2 = \left(\frac{g}{y}\delta y\right)^2 + \left(\frac{2g}{t}\delta t\right)^2$ quantified on the same sample.

Similar considerations apply to inertial sensing experiments with positronium atoms, in its either 2^3S [9] or Rydberg [32] long-lived states. Little experimentation has been performed so far with the external degrees of freedom of positronium [4]. Measuring optical forces (both dipolar and reactive), forces due to DC magnetic and electric gradients and ultimately gravitational forces with positronium are still open items of research. A detector as the one presented here, deployed on an existing long-lived positronium source with a Moiré deflectometer and a suitable ionization stage, would enable the detection of an acceleration of $\approx 10\,000$ m s^{-2} in a week of data taking, according to [9]. This would allow for more accurate charge neutrality tests of positronium, as well as measurements of its electric and magnetic dipole moment.

Several ways are being considered to enhance the spatial resolution, efficiency and detection surface of the current design. Minimizing the interdistance between the MCP

---

[20] Here *k* is a geometrical constant a-priori set by the experimental scheme chosen, e.g. $k = 0.5$ for free-fall in vacuum and $k = 1$ for a moiré deflectometer.

stack and TimePix3 will lead to more localized charge distributions at the detection plane. This will reduce the reconstructed charge quantization noise by making a better use of the 10 bit dynamics in the measurement of the time-over-threshold of active pixels, leading to a more accurate event centroiding reconstruction. The adoption of the TimePix3 chip variant employing through-silicon vias and bump-bonded connections would remove the ≈1 mm clearance limitation of the wire bonds connectors of the current version. Similarly would do the adoption of the new bump-bonded TimePix4 chip version as it will become available, featuring also a four-fold detection surface. Ultimately, the resolution will be limited by the MCP interchannel distance; MCPs down to 3 μm channels are commercially available. Furthermore, adopting MCPs with higher open area ratios than the current 58% would proportionally increase the maximum efficiency (90% OAR are commercially available).

Data availability statement

The data that support the findings of this study are available upon reasonable request from the authors.

Acknowledgments

ORCID iDs

L Glöggler https://orcid.org/0000-0003-0194-8680
Ł Kłosowski https://orcid.org/0000-0002-5463-5381
L Penasa https://orcid.org/0000-0003-3117-5826
M Piwiński https://orcid.org/0000-0001-5847-2578
L Povolo https://orcid.org/0000-0003-1451-1947
M Volponi https://orcid.org/0000-0002-5048-8708
M Zawada https://orcid.org/0000-0002-2826-5129

References

[1] Testera G *et al* 2015 The AEgIS experiment *Hyperfine Interact.* **233** 13–20

[2] Aghion S *et al* 2014 A Moiré deflectometer for antimatter *Nat. Commun.* **5** 4538

[3] Amsler C *et al* 2021 Pulsed production of antihydrogen *Commun. Phys.* **4** 19

[4] Cassidy D B 2018 Experimental progress in positronium laser physics *Eur. Phys. J.* D **72** 53

[5] Amsler C *et al* 2019 Velocity-selected production of 2^3S metastable positronium *Phys. Rev.* A **99** 033405

[6] Aghion S *et al* 2015 Positron bunching and electrostatic transport system for the production and emission of dense positronium clouds in vacuum *Nucl. Instrum. Methods Phys. Res.* B **362** 86–92

[7] Fajans J and Surko C 2020 Plasma and trap-based techniques for science with antimatter *Phys. Plasmas* **27** 030601

[8] Doser M *et al* 2012 Exploring the WEP with a pulsed cold beam of antihydrogen *Class. Quantum Grav.* **29** 184009

[9] Mariazzi S, Caravita R, Doser M, Nebbia G and Brusa R S 2020 Toward inertial sensing with a 2^3S positronium beam *Eur. Phys. J.* D **74** 79

[10] Kimura M *et al* 2013 Development of nuclear emulsions with 1 μm spatial resolution for the AEgIS experiment *Nucl. Instrum. Methods Phys. Res.* A **732** 325–9

[11] Fujiwara M C *et al* 2004 Three-dimensional annihilation imaging of trapped antiprotons *Phys. Rev. Lett.* **92** 065005

[12] Andresen G B *et al* 2012 Antihydrogen annihilation reconstruction with the ALPHA silicon detector *Nucl. Instrum. Methods Phys. Res.* A **684** 73–81

[13] Storey J *et al* 2013 Particle tracking at 4 K: the fast annihilation cryogenic tracking (FACT) detector for the AEgIS antimatter gravity experiment *Nucl. Instrum. Methods Phys. Res.* A **732** 437–41

[14] Czerwinski E *et al* 2017 Commissioning of the J-PET detector for studies of decays of positronium atoms *Acta Phys. Pol.* B **48** 1961

[15] Andresen G B *et al* 2009 Antiproton, positron and electron imaging with a microchannel plate/phosphor detector *Rev. Sci. Instrum.* **80** 123701

[16] Jones A C L *et al* 2016 Large-area field-ionization detector for the study of Rydberg atoms *Rev. Sci. Instrum.* **87** 113307

[17] Amsler C *et al* 2019 A ≈100 μm-resolution position-sensitive detector for slow positronium *Nucl. Instrum. Methods Phys. Res.* B **457** 44–48

[18] Caravita R *et al* 2020 Hybrid imaging and timing Ps laser excitation diagnostics for pulsed antihydrogen production *Acta Phys. Pol.* A **137** 96–100

[19] Vallerga J , Tremsin A, DeFazio J, Michel T, Alozy J, Tick T and Campbell M 2014 Optical MCP image tube with a quad Timepix readout: initial performance characterization *J. Instrum.* **9** C05055

[20] Vallerga J , McPhate J, Tremsin A and Siegmund O 2008 High resolution UV, alpha and neutron imaging with the Timepix CMOS readout *Nucl. Instrum. Methods Phys. Res.* A **591** 151–4

[21] Vallerga J , Raffanti R, Tremsin A, McPhate J and Siegmund O 2011 MCP detector read out with a quad Timepix at kilohertz frame rates *J. Instrum.* **6** C01049

[22] Tremsin A S and Vallerga J 2020 Unique capabilities and applications of microchannel plate (MCP) detectors with Medipix/Timepix readout *Radiat. Meas.* **130** 106228

[23] Poikela T *et al* (TimePix3 collaboration) 2014 A 65K channel hybrid pixel readout chip with simultaneous ToA/ToT and sparse readout *J. Instrum.* **9** C05013

[24] Burian P *et al* 2020 Ethernet embedded readout interface for Timepix3 *J. Instrum.* **15** C01037

[25] Zecca A, Bettonte M, Paridaens J, Karwash G P and Brusa R S 1998 A new electrostatic positron beam for surface studies *Meas. Sci. Technol.* **9** 409

[26] Vallerga J, McPhate J, Tremsin A S and Siegmund O 2008 Optically sensitive MCP image tube with a Medipix2 ASIC readout *Proc. SPIE* **7021** 702115

[27] Gatti E, Oba K and Rehak P 1983 Study of the electric field inside microchannel plate multipliers *IEEE Trans. Nucl. Sci.* **30** 1

[28] Turecek D , Jakubek J and Soukup P 2016 USB 3.0 readout and time-walk correction method for TimePix3 detector *J. Instrum.* **11** C12065

[29] Vinelli G, Ferragut R, Giammarchi M, Maero G, Romé M and Toso V 2020 Real-time monitoring of a positron beam using a microchannel plate in single-particle mode *J. Instrum.* **15** 11030

[30] Sala S, Ariga A , Ereditato A, Ferragut R, Giammarchi M, Leone M, Pistillo C and Scampoli P 2019 First demonstration of antimatter wave interferometry *Sci. Adv.* **5** 7610

[31] Storry C H *et al* (ATRAP collaboration) 2004 First laser-controlled antihydrogen production *Phys. Rev. Lett.* **93** 263401

[32] Cassidy D B and Hogan S D 2014 Atom control and gravity measurements using Rydberg positronium *Int. J. Mod. Phys.: Conf. Ser.* **30** 1460259